LAWRENCE
LIVERMORE
NATIONAL
LABORATORY

LLNL-JRNL-665624

Fluid Simulation of Particle and Heat Fluxes during Burst of ELMs on DIIID with BOUT++ code

T. Y. Xia, X. Q. Xu, M. Fenstermacher

December 19, 2014

Nuclear Fusion

Disclaimer

This document was prepared as an account of work sponsored by an agency of the United States government. Neither the United States government nor Lawrence Livermore National Security, LLC, nor any of their employees makes any warranty, expressed or implied, or assumes any legal liability or responsibility for the accuracy, completeness, or usefulness of any information, apparatus, product, or process disclosed, or represents that its use would not infringe privately owned rights. Reference herein to any specific commercial product, process, or service by trade name, trademark, manufacturer, or otherwise does not necessarily constitute or imply its endorsement, recommendation, or favoring by the United States government or Lawrence Livermore National Security, LLC. The views and opinions of authors expressed herein do not necessarily state or reflect those of the United States government or Lawrence Livermore National Security, LLC, and shall not be used for advertising or product endorsement purposes.

LLNL-JRNL-665624

Nonlinear Fluid Simulation of Particle and heat Fluxes during Burst of ELMs on DIII-D with BOUT++ code

T. Y. Xia[1,2,*] and X. Q. Xu[2]

July 21, 2015

[1]Institute of Plasma Physics, Chinese Academy of Sciences, Hefei, China

[2]Lawrence Livermore National Laboratory, Livermore, CA 94550, USA

*xiaty@ipp.ac.cn

Abstract

In order to study the distribution and evolution of the transient particle and heat fluxes during ELM bursts, a BOUT++ six-field two-fluid model based on the Braginskii equations with non-ideal physics effects is used to simulate pedestal collapse in divertor geometry. The profiles from the DIII-D H-mode discharge #144382 with fast target heat flux measurements are used as the initial conditions for the simulations. A flux-limited parallel thermal conduction is used with three values of the flux-limiting coefficient α_j, free streaming model with $\alpha_j = 1$, sheath-limit with $\alpha_j = 0.05$, and one value in between. The studies show that a 20 times increase in α_j leads to ~ 6 times increase in the heat flux amplitude to the both inner and outer targets, and the widths of the fluxes are also expanded. The sheath-limit model of flux-limiting coefficient is found to be the most appropriate one, which shows ELM sizes close to the measurements. The evolution of the density profile during the burst of ELMs of DIII-D discharge #144382 is simulated, and the collapse in width and depth of n_e are reproduced at different time steps. The growing process of the profiles for the heat flux at divertor targets during the burst of ELMs measured by IRTV (infrared television) is also reproduced by this model. The widths of heat fluxes towards targets are a little narrower, and the peak amplitudes are as twice as the measurements possibly due to the lack of a model of divertor radiation which can effectively reduce the heat fluxes. The magnetic flutter combined with parallel thermal conduction is found to be able to increase the total heat loss by around 33% since the magnetic flutter terms provide the additional conductive heat transport in the radial direction. The heat flux profile at both inner and outer targets is obviously broadened by magnetic flutter. The lobe structures near the X-point at LFS are both broadened and elongated due to the magnetic flutter.

1 Introduction

To assess the performance requirements of future tokamaks, such as ITER, one must study[1] discharges in the high edge particle and energy confinement regime known as H-mode [2]. In H-mode the steep pressure gradients can drive ballooning modes and bootstrap current generates peeling modes[3], and these two modes are considered to explain the trigger of Type-I edge-localized modes (ELMs) [4] successfully. However, unmitigated Type-I ELMs can lead to the impulsive heat and particle losses, which are predicted to cause excessive erosion and damage to plasma facing components (PFCs) in future tokamaks [5]. The nonlinear simulation of peeling-ballooning (P-B) modes is necessary to understand the ELM physics and find the methods to mitigate the heat flux problem to PFCs. SOLPS [6] and UEDGE [7] are widely used to simulate the steady-state energy depositions on divertor targets in the present and future tokamak design work. The transient heat fluxes during ELMs can be simulated with the modeled transport coefficients with SOLPS [8] and UEDGE. The self-consistent understanding of the transient evolution of ELMs is important and urgent to be studied.

The initial-value BOUT++ code has successfully simulated the nonlinear crash phase of ELMs [9, 10]. The latest BOUT++ studies show an emerging understanding of dynamics of edge localized mode (ELM) crashes

and the consistent collisionality scaling of ELM energy losses with the world multi-tokamak database [11]. The six-field two-fluid module has been developed to simulate the ELM crash in shifted-circular geometry [12, 13]. The typical values for transport coefficients in the saturation phase after ELM crashes are $D_r \sim 200\mathrm{m}^2\mathrm{s}^{-1}$, $\chi_{ir} \sim \chi_{er} \sim 40\mathrm{m}^2\mathrm{s}^{-1}$. The theoretical and simulation results of a gyro-Landau-fluid (GLF) extension of the BOUT++ code are summarized in Ref. [13, 14], which contributes to increasing the physics understanding of ELMs.

In this paper, the six-field two-fluid model is used in the divertor geometry of DIII-D ELMy H-mode discharge #144382. The paper is organized as follow. Sec. 2 is the introduction of the simulation model. Sec. 3 is the simulations setup with the measured geometry and profiles of DIII-D discharge #144382. The simulation results for the effects of flux-limited coefficient are explained in Sec. 4, as well as the validation with experimental measurements. Sec. 5 is the discussions about the effects of the magnetic flutter terms in parallel thermal conductions. The discussions of the model is also in this section. The last section is summary.

2 Six-field two-fluid model

In this paper, the electromagnetic six-field two-fluid module under BOUT++ framework are used to simulate the nonlinear evolution of ELMs in tokamak configuration. Starting from the Braginskii equations, within the flute-reduction, our six-field model is constituted of 6 evolving equations based on Ref. [15] and [12], which are written in drift ordering as

$$\begin{aligned}
\frac{\partial}{\partial t}\varpi &= -\frac{1}{B_0}\boldsymbol{b}\times\boldsymbol{\nabla}_\perp\Phi\cdot\boldsymbol{\nabla}\varpi - \frac{1}{B_0}\boldsymbol{b}\times\boldsymbol{\nabla}_\perp\phi\cdot\boldsymbol{\nabla}\varpi_0 + B_0^2\nabla_\parallel\left(\frac{J_\parallel}{B_0}\right) + 2\boldsymbol{b}\times\boldsymbol{\kappa}\cdot\boldsymbol{\nabla}p \\
&\quad -\frac{1}{2\Omega_i}\left[\frac{1}{B_0}\boldsymbol{b}\times\boldsymbol{\nabla}P_i\cdot\boldsymbol{\nabla}\left(\nabla_\perp^2\Phi\right) - Z_ieB_0\boldsymbol{b}\times\boldsymbol{\nabla}n_i\cdot\boldsymbol{\nabla}\left(\frac{\nabla_\perp\Phi}{B_0}\right)^2\right] \\
&\quad +\frac{1}{2\Omega_i}\left[\frac{1}{B_0}\boldsymbol{b}\times\boldsymbol{\nabla}\Phi\cdot\boldsymbol{\nabla}\left(\nabla_\perp^2P_i\right) - \nabla_\perp^2\left(\frac{1}{B_0}\boldsymbol{b}\times\boldsymbol{\nabla}\Phi\cdot\boldsymbol{\nabla}P_i\right)\right] + \mu_{\parallel i}\nabla_{\parallel 0}^2\varpi, \qquad (1)\\
\frac{\partial}{\partial t}n_i &= -\frac{1}{B_0}\boldsymbol{b}\times\boldsymbol{\nabla}_\perp\Phi\cdot\nabla n_i - \frac{2n_i}{B_0}\boldsymbol{b}\times\boldsymbol{\kappa}\cdot\boldsymbol{\nabla}\Phi \\
&\quad -\frac{2}{Z_ieB_0}\boldsymbol{b}\times\boldsymbol{\kappa}\cdot\boldsymbol{\nabla}P_i - n_iB_0\nabla_\parallel\left(\frac{V_{\parallel i}}{B_0}\right), \qquad (2)\\
\frac{\partial}{\partial t}V_{\parallel i} &= -\frac{1}{B_0}\boldsymbol{b}\times\boldsymbol{\nabla}_\perp\Phi\cdot\boldsymbol{\nabla}V_{\parallel i} - \frac{1}{m_in_{i0}}\boldsymbol{b}\cdot\boldsymbol{\nabla}P, \qquad (3)\\
\frac{\partial}{\partial t}T_i &= -\frac{1}{B_0}\boldsymbol{b}\times\boldsymbol{\nabla}_\perp\Phi\cdot\boldsymbol{\nabla}T_i - \frac{2}{3}T_i\left[\left(\frac{2}{B_0}\boldsymbol{b}\times\boldsymbol{\kappa}\right)\cdot\left(\boldsymbol{\nabla}\Phi + \frac{1}{Z_ien_{i0}}\boldsymbol{\nabla}P_i + \frac{5}{2}\frac{k_B}{Z_ie}\boldsymbol{\nabla}T_i\right) + B_0\nabla_\parallel\left(\frac{V_{\parallel i}}{B_0}\right)\right] \\
&\quad +\frac{2}{3n_{i0}k_B}\nabla_\parallel\left(\kappa_{\parallel i}\nabla_\parallel T_i\right) + \frac{2m_e}{m_i}\frac{Z_i}{\tau_e}\left(T_e - T_i\right), \qquad (4)\\
\frac{\partial}{\partial t}T_e &= -\frac{1}{B_0}\boldsymbol{b}\times\boldsymbol{\nabla}_\perp\Phi\cdot\boldsymbol{\nabla}T_e - \frac{2}{3}T_e\left[\left(\frac{2}{B_0}\boldsymbol{b}\times\boldsymbol{\kappa}\right)\cdot\left(\boldsymbol{\nabla}\Phi - \frac{1}{en_{e0}}\boldsymbol{\nabla}P_e - \frac{5}{2}\frac{k_B}{e}\boldsymbol{\nabla}T_e\right) + B_0\nabla_\parallel\left(\frac{V_{\parallel e}}{B_0}\right)\right] \\
&\quad +0.71\frac{2T_e}{3en_{e0}}B_0\nabla_\parallel\left(\frac{J_\parallel}{B_0}\right) + \frac{2}{3n_{e0}k_B}\nabla_\parallel\left(\kappa_{\parallel e}\nabla_\parallel T_e\right) - \frac{2m_e}{m_i}\frac{1}{\tau_e}\left(T_e - T_i\right) + \frac{2}{3n_{e0}k_B}\eta_\parallel J_\parallel^2. \qquad (5)\\
\frac{\partial}{\partial t}A_\parallel &= -\nabla_\parallel\phi + \frac{\eta}{\mu_0}\nabla_\perp^2A_\parallel + \frac{1}{en_{e0}}\nabla_\parallel P_e + \frac{0.71k_B}{eB_0}\nabla_\parallel T_e - \frac{\eta_H}{\mu_0}\nabla_\perp^4A_\parallel, \qquad (6)
\end{aligned}$$

The variables in these equations are defined as

$$\begin{aligned}
\varpi &= n_{i0}\frac{m_i}{B_0}\left(\nabla_\perp^2\phi + \frac{1}{n_{i0}}\nabla_\perp\phi\cdot\nabla_\perp n_{i0} + \frac{1}{n_{i0}Z_ie}\nabla_\perp^2p_{i1}\right), \qquad (7)\\
J_\parallel &= J_{\parallel 0} - \frac{1}{\mu_0}\nabla_\perp^2A_\parallel, \qquad (8)\\
V_{\parallel e} &= V_{\parallel i} + \frac{1}{\mu_0Z_ien_i}\nabla_\perp^2A_\parallel. \qquad (9)
\end{aligned}$$

Notice that the third term on the right hand side of Eq. (1) should be $2\boldsymbol{b}\times\boldsymbol{\kappa}\cdot\boldsymbol{\nabla}p$, which has typos in Ref. [12]. The Kelvin-Helmholtz term, which is expressed as $\frac{1}{B_0}\boldsymbol{b}\times\boldsymbol{\nabla}_\perp\phi\cdot\boldsymbol{\nabla}\varpi_0$ in Eq. (1), is added into this model, where $\varpi_0=\boldsymbol{b}_0\cdot\boldsymbol{\nabla}\times\boldsymbol{V}_{0net}$ and $\boldsymbol{V}_{0net}$ is the net equilibrium flow. In this model, all the variables can be written as $F=F_0+F_1$, where F_0 represents for the equilibrium part of arbitrary field quantity and F_1 is the perturbed component. Here $A_\parallel$ is the perturbed parallel vector potential, $\mathbf{b}=\mathbf{b}_0+\mathbf{b}_1=\mathbf{b}_0+\boldsymbol{\nabla}A_\parallel\times\mathbf{b}_0/B$ is the unit vector of the total magnetic field, $\boldsymbol{\kappa}=\mathbf{b}_0\cdot\bigtriangledown\mathbf{b}_0$. The definition of pressure in this model is $P_j=P_{j0}+p_{j1}=k_Bn_jT_j$, $p_{j1}=k_B(n_{j0}T_{j1}+n_{j1}T_{j0}+n_{j1}T_{j1})$ for j species. $\mathbf{V}_E=(\mathbf{b}_0\times\nabla_\perp\Phi)/B_0$, and $\Phi=\Phi_0+\phi$ is the total electric potential. Notice that $V_{\parallel i}$, $V_{\parallel e}$ and ϖ only have perturbed part. Here $\Omega_i=Z_ieB/m_i$ is the ion gyro frequency, $\nabla_\parallel=\nabla_{\parallel 0}-\boldsymbol{b}_0\times\boldsymbol{\nabla}A_\parallel/B_0$, $\boldsymbol{\nabla}_\perp=\boldsymbol{\nabla}-\boldsymbol{b}\nabla_\parallel$ and $\nabla_{\parallel 0}=\boldsymbol{b}_0\cdot\boldsymbol{\nabla}$.

In this model, the pressure is assumed to be isotropic, so $\mu_{\parallel i}\nabla_{\parallel 0}^2\varpi$ is the simple form of parallel viscosity and perpendicular viscosity is neglected in our model. Here η is defined as the parallel Spitzer resistivity, $\eta_{SP}=0.51\times1.03\times10^{-4}Z_ilnAT^{-3/2}\Omega\cdot$m. Although hyper-resistivity η_H, also known as electron viscosity, is generally negligibly small in collisional plasmas, it can be significant in a collisionless plasma. From nonlinear simulations we have found that the P–B modes trigger magnetic reconnection, which drives the collapse of the pedestal pressure. The ELM dynamics involves multi-scale interaction between low-n MHD peeling-ballooning mode and electron scale turbulence. For practical simulation purpose, hyper-resistivity can be used to set the finest resolved radial scale in simulations for facilitating magnetic reconnection [16]. Either resistivity η or hyper-resistivity η_H can break the frozen-in flux constraint of ideal MHD theory. The electron inertial is considered to be one of the mechanism to generate the self-consistent hyper-resistivity[17]. In this paper, a non-self-consistent hyper-resistivity with $S_H=10^{13}$, which is used in the following sections, is available to get through the nonlinear crash of ELM and does not generate hyper-resistive ballooning modes. The Spitzer-Härm parallel thermal conductivities are defined as $\kappa_{\parallel i}=3.9n_iv_{th,i}^2/\nu_i$ and $\kappa_{\parallel e}=3.2n_ev_{th,e}^2/\nu_e$, where $v_{th,j}$ is the thermal velocity for j particle and ν_j is the collision rate. Since in hot pedestal the collisionality is low and this classic $\kappa_{\parallel j}$ is not valid to describe the weakly collisional plasmas, the free-streaming expression $\kappa'_{fs,j}=\alpha_j\kappa_{fs,j}=\alpha_jn_jv_{th,j}qR_0$, is taken into account of kinetic effects. Here q is the local safety factor and α_j is the flux-limited coefficients, which will be discussed in Sec. 4.2. When $\alpha_j=1$, the free-streaming thermal conduction $\kappa'_{fs,j}$ means that the particle transport through the connection length without collision. The kinetic effect is traditionally introduced by limiting the heat flux by a fraction of the free streaming flux. Kinetic effects are typically included in fluid transport codes in the form of the harmonic average 'flux limiting' expressions [18]. Ref. [19] indicates that in weakly collision regime, the flux-limited heat flux shows the good approximation to the Fokker-Planck model. Therefore, in the edge simulation, where bridges the low collision region to high collision one, the effective thermal conductivities are written as

$$\kappa_{eff,j} = \frac{\kappa_{\parallel j}\kappa'_{fs,j}}{\kappa_{\parallel j}+\kappa'_{fs,j}}. \tag{10}$$

Within this form, $\kappa_{eff,j}$ is determined by $\kappa_{\parallel j}$ at the bottom of pedestal region where plasmas are in collisional limit, and is dominant by $\kappa_{fs,j}$ in long mean free path condition. The parallel diffusion terms should be evaluated along the total magnetic field lines. In the most part of this paper, only the equilibrium magnetic field lines are considered in the thermal conduction terms unless mentioned, meaning just $\nabla_{\parallel 0}\left(\kappa_{\parallel j}\nabla_{\parallel 0}T_j\right)$ is kept in Eq. (4) and (5). The effects of the magnetic flutter in thermal conduction will be discussed in Sec. 5. Notice that the perpendicular classical diffusivities are neglected here because in this typical P-B unstable equilibrium, $\kappa_\perp\ll\kappa_\parallel$. Therefore, we believe that the radial diffusion will not affect the simulation results in the linear phase and even in the early nonlinear phase, which we will discuss in this paper, but in the late nonlinear phase, $\kappa_\perp$ may be important to transport and turbulent processes on transport time scale.

The terms in two square brackets in Eq. (1) represent the gyro-viscous terms brought in by the finite ion Larmor radius (FLR) effects. These terms are necessary for two-fluid models to keep the whole FLR stabilizing effects when ion density gradient is steep and temperature is high [14, 20]. In this paper, the net equilibrium zonal flow is set to be zero.

The Eqs. (1) - (9) are solved using the field aligned (flux) coordinate system (x,y,z) with the shift radial derivatives [21]. In this coordinate system x is the radial direction and defined as $x=(\Psi-\Psi_{axis})/(\Psi_{separatrix}-\Psi_{axis})$, which is the normalized poloidal flux and Ψ is the poloidal magnetic flux, y is the parallel direction with a twisted-shift boundary condition and z is the binormal direction. Hereafter, we use $\Psi_N=x$ to represent the normalized magnetic flux for simplification.

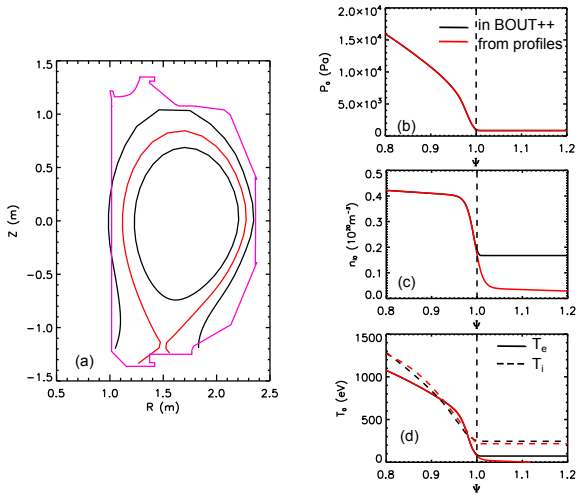

Figure 1: (a): The simulation domain of DIII-D ELMy H-mode discharge 144382. The region between two black curves is the simulation domain in this paper. The red curve is the separatrix and the magenta curves show the first wall of device. (b): The pressure profiles. (c): The density profiles. (d): The temperature profiles in the simulations. In these three panels, the black curves are used in the simulation which is interpolated from the experimental measured one in red. In panel (d), the solid curves are T_e and the dashed are T_i.

3 DIII-D equilibrium

In this paper, the equilibrium of DIII-D ELMy H-mode discharge No. 144382 is used for the simulations. The discharge parameters are $I_P = 1.16$MA, $B_T = 2.15$T, average $P_{NBI} = 5.8$MW, $R = 1.78$m, $a = 0.58$m, $\kappa = 1.72$ and $q_{95} = 4.0$ [22]. The geometry of this discharge is lower single-null and the triangularity is low ($\delta = 0.35$). The ELM frequency at the stationary phase is $f_{ELM} \sim 150$Hz. The constant normalized beta, $\beta_N = 1.9$ and steady density are held by input power feedback during the ELMs. The crash and recovery of the small Type-I ELM at 2544.5ms were detected with multiple fast acquisition data chords in the pedestal, scrape-off layer (SOL) and divertor. This ELM produced a drop in the plasma stored energy of 2% (17kJ from a 0.8MJ plasma). The fast target heat flux measurements by infrared television (IRTV) at 12kHz are also applied in this discharge to get the evolution of the heat flux on targets during the ELM cycle, so it is convenient to validate our model.

Fig. 1 shows the domain and the profiles in the simulations. Panel (a) shows that the geometry of discharge #144382 is a lower single-null magnetic configuration. The simulation domain is shown be the region between two black curves, which covers the pedestal region and SOL from $\Psi_N = 0.8$ to $\Psi = 1.2$. For computational efficiency, only one eighth of the torus is simulated in this work. The red curve shows the separatrix and the peak pressure gradient is located at $\Psi_N = 0.978$. The first wall of the device are drawn by the magenta curves. Panel (b) shows the comparison between the measured pressure profile from experiments (black) and P_0 used in the simulation (red). The experimental pressure profile is obtained from the kinetic EFIT equilibrium [23]. After the interpolation in the simulation domain, the red curve is almost the same as the black one. Because there is no information of pressure outside the separatrix from kinetic EFIT equilibrium, the profile outside the separatrix is assumed to be zero gradient for pressure, densities and temperatures. The parallel current is assumed to be zero outside the separatrix. Panel (c) shows the profile of electron density n_e and Panel (d) shows the electron temperature T_e (solid curves) and ion temperature T_i (dashed). The black curves represent the profile used in the simulation and the red are from the measurements for these two panel. The profiles of n_e and T_e are interpolated from the experimental measurements and $T_i = P_0/(kn_e) - T_e$, where P_0 is exactly same as in g-file. The reason why the measured T_i is not used is because in our model, the quasi-neutral condition $n_i = n_e$ is assumed and there is no impurities considered in the simulation domain during the evolution of ELMs. Panel (d) shows that the derived T_i is close to the measurements. In this paper, the inner boundary conditions on x direction, where $\Psi_N = 0.8$, are $\partial n_i/\partial\psi = 0$, $\partial T_j/\partial\psi = 0$, $V_{\|i} = 0$, $\varpi = 0$, $\nabla_\perp^2 A_\| = 0$, $\partial^2\phi/\partial^2\psi = 0$. For outer boundary, where $\Psi_N = 1.2$, $n_i = 0$, $T_j = 0$, $V_{\|i} = 0$, $\varpi = 0$, $\nabla_\perp^2 A_\| = 0$, $\partial^2\phi/\partial^2\psi = 0$. The domain of y directions inside the separatrix is twisted-shifted periodic and z is periodic. The boundary conditions not mentioned here are all set to be Neumann.

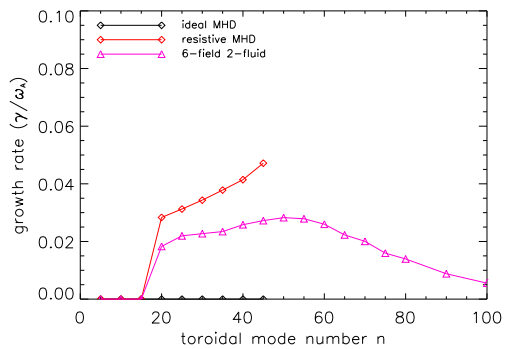

Figure 2: The linear growth rate of discharge #144382. The black-triangle curve which is overlapped by the x-axis shows the ideal MHD results. The red-diamond curve shows the ideal MHD + Spitzer resistivity. The magenta-triangle curve is the linear growth rate calculated by 6-field model. This figure shows that the ELM of #144382 is consistent with resistive-ballooning in the model.

4 Simulation Results

4.1 Linear analysis

The linear instability of DIII-D ELMy H-mode discharge usually determines the characteristic of ELM [3]. The black-triangle curve in Fig. 2 shows the spectrum of the linear growth rate calculated with the ideal P-B model in BOUT++. For all the toroidal mode number n, the linear growth rate $\gamma = 0$, which means that this discharge is stable for ideal P-B mode. When Spitzer resistivity is considered, the instabilities appear when $n \geq 20$. Therefore, this discharge is unstable for resistive ballooning mode. The linear growth rate calculated by 6-field model with all the non-ideal physics except thermal conductions are shown as the magenta-triangle curve in Fig. 2. The growth rates at $n > 50$ are decreased due to the ion diamagnetic stabilizing effects. The peak growth rate is around $n = 50$. The experimental measurements indicate that this is a small ELM event. This small ELM event is very close to the ideal P-B instability threshold, therefore it is sensitive to both the equilibrium profiles and physics models. First, the small error from the profile measurements leads to the uncertainty to determine if unstable modes are ideal or resistive in the actual experiments. Second, in this simulation, the pressure in the g-file has the large impurity contribution. However, in our physics model Eqs. (1) - (6), only ion and electron species are kept and the impurity is dropped. From the equilibrium profiles derived from measurements, if the total pressure is just the sum of ion and electron pressures, the gradient of pressure is $\sim 10\%$ larger than that in the g-file which takes the impurity profile into the account.

4.2 The effects of flux-limited coefficient α_j

As mentioned in Sec. 2, the parallel thermal conduction plays as the key role of the heat transport in SOL. The classical Spitzer-Härm model can significantly overestimated or underestimate particle and heat fluxes

to the divertor targets [24, 25]. Therefore, the kinetic effects are necessary to describe the parallel thermal conduction in SOL when ELMs occur. One of the simple method to implement the kinetic modification is the flux-limited expression for the parallel thermal conduction. The flux-limited coefficient α_j is used to address the constant fraction of the limited heat flux to the free streaming value, where $j \in \{i, e\}$ and the value ranges in $\alpha_j \in [0.03, 3]$ [18]. Ref. [19] compares the Landau-fluid non-local parallel electron heat transport in low collisionality regime, which is represented by a sum of Lorentzians [26], to the flux-limited expression and gets the consistent results. This comparison shows that the flux-limited coefficient with the range of $\alpha_e \in [0.15, 0.3]$ get at least 18 $\sim$ 40% larger amplitude of the parallel heat flux than the Landau-fluid or Fokker-Planck model. Since the previous work only gave a wide range of the value, the flux-limited coefficient α_j is chosen as a calibration parameter in our model. However, for fluid simulations, the value of α_j can affect the amplitudes of the heat flux in SOL dramatically, so it is necessary to know the exact α_j in the SOL and divertor heat flux studies. In this subsection, the scan of α_j is performed to find the appropriate value for the DIII-D simulations. For simplicity, we assume $\alpha_i = \alpha_e = \alpha_j$, and set the range from the sheath limit $\alpha_j^{SH} \simeq 2.5\left(\frac{T_i}{T_e} + Z_i\right)^{\frac{1}{2}} (\frac{m_e}{m_i})^{\frac{1}{2}} \simeq 0.05$ to the free-streaming limit $\alpha_j^{FS} = 1$ [18]. Besides these two limiting values, $\alpha_j = 0.1$ inside the range is also chosen for the comparisons.

Fig. 3(a) shows the influence of α_j on the total energy loss. The y-axis is the ELM size, which is defined as the ratio of the energy loss due to an ELM to the total energy stored by plasma. For this discharge, the total energy measured from experiment is 0.8MJ [22]. This figure shows the trend that the ELM size becomes larger with larger flux-limited coefficient α_j. Notice that the ELM size is calculated at $t = 0.3$ms and averaged from $t = 0.29$ to 0.31ms since the energy loss is difficult to get saturated in this simulation. The reason will be discussed in Sec. 4.3. This is because α_j is correlated with the effective thermal conductivity $\kappa_{eff,j}$ based on Eq. (10), so larger α_j also means larger diffusion along field lines, which are shown in Fig. 3(b). Here the flux-limited thermal conduction dominates $\kappa_{eff,j}$ through the whole simulation domain, including in the SOL. The reason is that we assume that the density and temperature profiles in SOL to be zero-gradient, which leads to lower collisionality. Therefore, the collisionality in SOL is still not large enough to make the Spitzer-Härm thermal conductivity dominant. Although the thermal conduction can suppress large ELMs which has been discussed in the circular geometry based on the simple five-field two fluid model[27], the radial transport to SOL becomes more important for the nonlinear simulation on transport time scale in this more complicated model and geometry. In order to understand the reason, the averaged radial energy fluxes are calculated by the definition as

$$Q_{jr} \quad = \quad < p_j V_r >= \left\langle n_j T_j \frac{(\boldsymbol{b}_0 \times \boldsymbol{\nabla}\Phi)_r}{B_0} \right\rangle + \left\langle \kappa_{||j} \frac{\boldsymbol{b}_0 \times \boldsymbol{\nabla} A_\parallel}{B_0} \cdot \boldsymbol{\nabla} T_j \right\rangle . \tag{11}$$

The radial particle fluxes can be similarly defined as

$$\Gamma_{ir} \quad = \quad < n_i V_r >= \left\langle n_i \frac{(\boldsymbol{b}_0 \times \boldsymbol{\nabla}\Phi)_r}{B_0} \right\rangle + \left\langle \frac{J_\parallel}{Z_i e} \cdot \left(\frac{\boldsymbol{b}_0 \times \boldsymbol{\nabla} A_\parallel}{B_0} \right)_r \right\rangle , \tag{12}$$

In both definitions, the first term is derived from the radial component of E×B drift, or named as convective component. The second term of Eq. (11) is the radial energy flux induced by the magnetic flutter in parallel energy flux $Q_{\parallel j}$, or called conductive component. The second term of Eq. (12) is from the radial component of the perturbed magnetic field in parallel particle flux contribution. As shown in Panel (a) of Fig. 4, the averaged profiles of the flux averaged electron radial energy fluxes after $t = 200\mu$s are plotted . The black curves are derived with $\alpha_j = 0.05$, red $\alpha_j = 0.1$ and blue $\alpha_j = 1.0$. The solid curves mean the radial energy flux induced by E×B drift and the solid curves represent the radial component of $q_{\parallel j}$. This figure shows that the radial energy flux is increased with α_j for both the conductive and convective components from the position of the peak pressure gradient to the separatrix. This behavior means that more energy is lost from the pedestal region into the SOL with larger α_j, and then goes along the field line to the divertor targets. The panel (b) of Fig. 4 shows the α_j scan for the ion radial energy fluxes and the result is similar to electron. Therefore, the ELM size with larger α_j becomes larger, as shown in Fig. 3. This result is different from the conclusion in Ref. [27], because of two reasons. First, the ELM event is quite large in Ref. [27], and the ELM size is above 10%, which is much larger than the value shown in Fig. 3(a). The thermal conductivities play as the dominant role in that circular equilibrium and they can effectively suppress the perturbation in the region of peak pressure gradient. In this DIII-D equilibrium, the ELM size is small and the dominant

(a) (b)

Figure 3: (a) The ELM size of different flux-limited coefficients α_j. Larger α_j leads to larger ELM size. (b) The radial profiles for thermal conductivity $\kappa_{\parallel e}$ at the start of the simulation. The purple curve is the thermal conductivity calculated from Spitzer-Härm model without any modification of flux-limited expression. The black is with the flux-limited coefficient $\alpha_j = 0.05$, the red is $\alpha_j = 0.1$ and blue $\alpha = 1.0$.

radial transport is mainly E×B convection. The $\kappa_{\parallel j}$ suppressing effects are not as obvious as that in Ref. [27]. Second, there is no open field lines in the circular geometry. The larger thermal conduction in SOL means fast parallel transport of energy along field lines and it is effective to transport energy out of pedestal due to magnetic flutter. While in circular case, this loss mechanism is absent without the open field lines.

In Fig. 4, compared with the convective and conductive components of the radial energy fluxes, it is found that α_j can affect the relative magnitude between them. For ions, the radial energy fluxes are dominated by the convective term, and the conductive fluxes are two orders of magnitude smaller for all the tested flux-limited coefficients. However, for electrons, when $\alpha_j = 1.0$, the conductive flux (the blue dashed curve) becomes larger than the convective component (the blue solid curve), especially inside the separatrix. For $\alpha_j = 0.1$ and 0.05, the convective fluxes are still dominant. The electron thermal conductivity is more than one order of magnitude larger than the ion thermal conductivity, so the impact on electrons is more sensitive than that on ions. The larger thermal conductivity means larger parallel energy flux, and larger radial transport due to magnetic flutter, while the convective fluxes from the E×B drift is not affected. This trend is shown by the dashed curves in both panels of Fig. 4. Therefore, when α_j is large enough in this DIII-D equilibrium, such as the free-streaming limit $\alpha_j = 1.0$ in this paper, the amplitude of the convective flux can be exceeded by the conductive component.

The comparisons of the profiles at the outer mid-plane with different flux-limited coefficient α_j are shown in Fig. 5. From the three panels, it is easy to see that the T_e profile is the most sensitive to α_j, and T_i and n_e are less sensitive because the thermal conductivities play the most important role in these simulations. In Panel (a) of Fig. 5, n_e shows the similar profiles for different α_j because the thermal conductions does not affect the continuity equation and the small differences are mainly caused by the E×B drift. The ion temperature T_i profiles in Panel (b) show some differences at the inner boundary. The large α_j, or $\kappa_{\parallel j}^{eff}$ prevents the perturbations from propagating to the inner side of the peak pressure gradient region. The concentration of the perturbations inside the peak gradient region generates large turbulent transport, which leads to more obvious T_j drop than the equilibrium profile. This conclusion is consistent with Ref. [27]. For

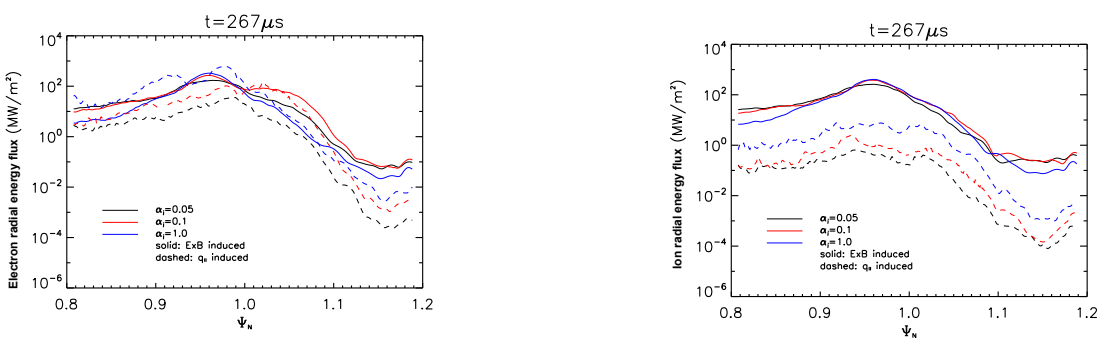

(a) (b)

Figure 4: Panel (a): The profiles of the radial electron energy fluxes with different α_j at $t = 267\mu$s. Panel (b): The profiles of the radial ion energy fluxes with different α_j. The solid curves represent the radial energy fluxes induced by E×B drift (convective component) and the dashed curves are induced by the radial component of the parallel energy fluxes (conductive component). At the peak gradient region to the separatrix, the larger α_j shows the larger radial energy flux which means more energy flows out of the separatrix to SOL.

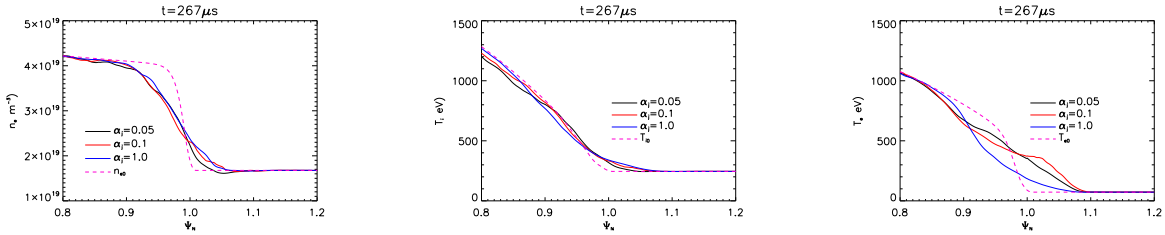

(a) (b) (c)

Figure 5: (a): The electron density profiles at the outer mid-plane for different α_j at $t = 267\mu$s. (b): The ion temperature profiles. (c): The electron temperature profiles. The black curves are calculated with $\alpha_j = 0.05$, the red curves are $\alpha_j = 0.1$ and blue are $\alpha_j = 1.0$. The dashed magenta curves means the initial profiles in our simulations which are derived from experimental measurements.

electron temperature T_e, all the perturbations can not propagate to the inner boundary because $\kappa_{\|e}^{eff}$ is much larger than $\kappa_{\|i}^{eff}$. In the pedestal foot region between the position of the peak pressure gradient position and the separatrix, the profile is lower with larger α_j, because the larger radial energy flux transports more energy to the SOL which has been explained in the previous paragraph.

Fig. 6 shows the correlation between heat flux to divertor targets and the flux-limited coefficient α_j. Panel (a) shows the radial distribution of the heat fluxes and Panel (b) is the time evolution of the heat fluxes to targets. In Panel (a), all of the heat fluxes are distributed outside the separatrix for both inner and outer target. It is not surprising that the amplitude of the heat flux is correlated with the value of α_j, since the heat fluxes on targets are dominated by the parallel transport along the magnetic field line. The ratio of the amplitudes of the heat fluxes to the outer target is $q(\alpha_j = 1.0) : q(\alpha_j = 0.1) : q(\alpha_j = 0.05) = 6.26 : 1.38 : 1.00$, and at the inner target the ratio is $q(\alpha_j = 1.0) : q(\alpha_j = 0.1) : q(\alpha_j = 0.05) = 6.31 : 2.36 : 1.00$. A factor of 20 α_j variation leads to about 6 times difference in heat flux on both targets. The width of the heat fluxes is also expanded more widely with larger α_j, because the radial energy fluxes are still larger near the separatrix.

After all, the value of α_j in our model is very important to describe the amplitudes of the heat fluxes towards targets and it is necessary to calibrate α_j with the experiments. For this DIII-D discharge #144382, the ELM size was measured as 2% of the total stored plasma energy. From Fig. 3, the case of the sheath limit value $\alpha_j = 0.05$ shows the closest result. For the heat flux measurement, the peak value at the outer target after 200μs of the ELM burst is around 300W/cm^2. The closest simulation result is also the sheath limit case with the peak value ~ 500W/cm^2. As a conclusion, from this simulation of the heat flux to divertor targets with the absence of the neutral particles and the radiation effects, the sheath limited flux-limited parallel thermal conduction is the most acceptable one. From now on in this paper, $\alpha_j = 0.05$ is used for all the simulations.

4.3 Validations with measurements and discussions

As discussed in Sec. 4.2, the sheath model of flux-limited thermal conduction $\alpha_j = 0.05$ are used to simulate the sheath effects of the targets. Within this model the total energy loss is obtained as 18kJ which is very close to the measured value of 17kJ. This conclusion is different from Ref. [28] which shows that the free-streaming model of parallel thermal conduction is consistent with the kinetic simulations for Type-I ELMs. The most important reason is that we simulate the self-consistent 3D parallel and perpendicular transport with ELM dynamics, including the E×B convection and magnetic flutter, while in Ref. [28], only one spatial

(a) (b)

Figure 6: (a): The comparison of the radial distribution of heat fluxes to divertor targets 200μs after the burst of ELM with different α_j. (b): The time evolution of the heat fluxes to targets. The dashed curves are for the inner target and the solid curves are for outer target. For both panels, black curves represent the case $\alpha_j = 0.05$, red are $\alpha_j = 0.1$ and blue are $\alpha_j = 1.0$. The larger α_j leads to larger heat flux to targets.

dimension in the parallel direction is simulated and the cross-field transport rate is simply modeled by the sound speed at pedestal divided by the characteristic length of parallel direction. As discussed in Sec. 4.2, the radial transport induced by both E×B and magnetic flutter during ELM is closely correlated with α_j. For larger α_j, the more total pedestal energy is transported into the SOL by ELMs, which increases the heat flux amplitude. The second reason is that the equilibrium in Ref. [28] derived from JET shows quite high temperature $T_{ped} = 1500$eV, while this DIII-D discharge has $T_{ped} \simeq 200$eV. Therefore, the lower temperature, which also means the higher collisionality, leads to the larger deviation from the free-streaming transport.

Fig. 7 shows the evolution of the electron density profiles n_e at outer mid-plane after the start of ELM [22]. Panel (a) is the measured profiles at the start of the ELM event, 0.29ms and 0.35ms after the ELM crash. Panel (b) is the simulated n_e profiles at the same time interval after the start of ELM event. In both panels, the black curves represent the initial profile at the start of the ELM. The magenta curves are for the n_e at 0.29ms after the ELM start and red are at 0.35ms. The simulation shows the similar crash range that the profile drops to the inner boundary $\Psi_N = 0.8$ or $\rho_N = 0.89$. The difference from the measurement is mostly because that the density profile is measured at 3007.1ms, which is different from the equilibrium reconstructed at 2544.5ms, the initial n_{e0} is not exactly the same as the simulation.

Fig. 8 shows the evolution of the profiles of the heat flux to the lower target during the ELM event for the simulated discharge [22]. Panel (a) is derived by the fast target heat flux measurements of 12kHz IRTV. Panel (b) is obtained from the six-field two-fluid model described in previous sections. The magenta curves for both panels are the heat flux profiles at the start of ELM. The black curves are at 200μs after the ELM burst, the red are at 280μs and the blue at 370μs. At the outer target, the simulated peak heat fluxes show the similar expansion to the measurements, from the strike point at $R \simeq 1.56$m to $R \simeq 1.65$m. The increasing progress of the peak heat flux is also shown in the simulation. The peak value keeps growing from the magenta curves to black, red and blue in both panels. The magenta curve in Panel (b) is too small to be seen because there is no energy flow into the SOL at the beginning of the simulation. The out-moving of the peak position at outer target is observed in our model. In panel (a), the peak of the heat flux is moved to $R \simeq 1.62$m for the blue curve from the strike point at $R \simeq 1.56$m for the black and magenta curves. In Panel (b) this out-moving effect is not so obvious as Panel (a) because the magnetic flutter terms in parallel thermal conductions, which are able to broaden the heat flux distribution, is not fully considered in this simulation yet. The effects about the magnetic flutter terms will be shown in Sec. 5. The present model leads to $\sim 40\%$ narrower of the width of the heat flux to outer target than the measurements. The amplitudes of the simulated heat fluxes in Fig. 8(b) are as twice as the measured values because there are only ions and electrons in our simulation. The low-temperature neutrals and impurities near the targets are not taken into consideration in this model, which can effectively dissipate the incoming energy flow through radiation and recombination. Therefore, the heat fluxes simulated here is the amplitude towards the targets and they should be much higher than the measurements. The amplitudes of the heat fluxes in the private flux region between the inner and outer separatrix in Panel (a) are due to reflections in the IRTV, which have been significantly reduced in the 2013 DIII-D campaign. There should be very low heat loads here, which is correctly simulated in Panel (b). The reason why the simulated heat fluxes at inner target show the similar amplitudes to measurements is that the reflection influences the precision for small fluxes, so the peaks at

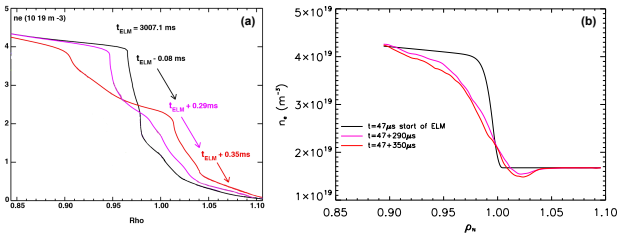

Figure 7: (a) The measured evolution of the density profiles at outer mid-plane during the crash of ELM. (b) The simulated evolution of the density profiles at the same time as Panel (a). The crash region of the density is well repeated by the simulation.

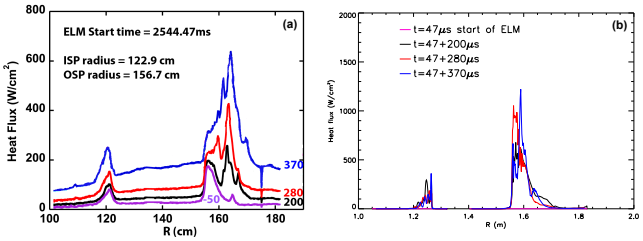

Figure 8: (a) The measured evolution of the heat flux profiles on lower targets during the burst of ELM event of DIII-D discharge #144382. (b) The evolution of the heat flux profiles obtained from BOUT++ simulation. The simulation derives the similar heat flux expansion on targets. The amplitudes are larger than the measurements because there are no neutrals and impurities in the model.

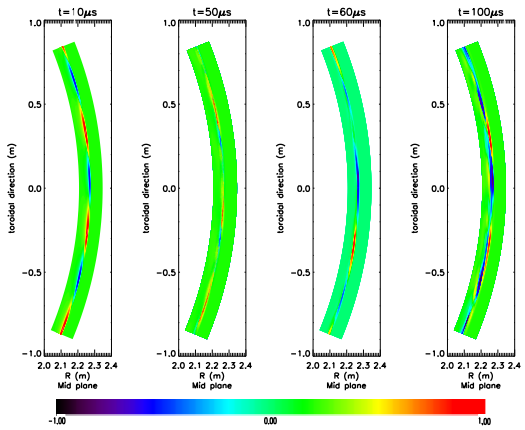

Figure 9: The evolution of the toroidal structure of T_{e1} at outer mid-plane during the burst of ELM. The four slices show the structures at $t = 10$, 50, 60 and 100μs after the start of the simulation. The evolution of the linear filaments to nonlinear filaments are represented. The peak amplitudes here are normalized to 1.

inner target in Panel (a) should be smaller. Another possible reason is that the simulated heat flux at inner target is underestimated because the magnetic flutter terms in thermal conduction are not considered in Panel (b) which are able to increase the inner heat flux.

One possible reason that the simulated energy loss is always larger than the measured value is the lack of energy and particle input in the simulation domain. As mentioned in Sec. 3, the inner boundary condition applied in the simulation sets no flux flowing into the pedestal region, so there is no additional source in this model. However, in the experiments, the auxiliary heating, such as NBI and RF, is necessary to maintain H-mode. This indicates that the additional particle and energy source should be considered in the ELM simulations. One simple method to consider the external source is to add the particle and energy flux via the inner boundary condition. This flux-driven boundary condition is able to prevent the fluctuations propagating into the inner boundary. When the fluctuations grow to the inner boundary with the zero-flux boundary condition, the energy stored near the boundary will be lost outwards to the separatrix and no mechanism could stop the lost. Therefore, the total energy loss will keep growing slowly and be very difficult to get saturated. The external source at the inner boundary might be able to constraint the slowly increasing of the total energy loss and obtain the smaller simulated energy loss. Another possible effect of the flux-driven boundary condition is to solve the issue that the simulated ELM bursts faster than the experiments. As shown in Fig. 7 and 8, both the crash of n_e and the increase of heat flux before 200μs are much faster than the measurements. The particle flux-driven boundary can bring additional particles into pedestal and may slow down the crash of n_e. Similarly, the energy flux-driven boundary may decrease the energy loss and slow down the heat flux growing at the beginning of the ELM burst near targets. The implementation of the flux-driven boundary condition will be our next-step work.

The evolution of the toroidal structures of perturbed electron temperature T_{e1} at outer mid-plane are shown in Fig. 9. As mentioned in the previous section, one eighth of the whole torus is plotted here. The first slice is the initial linear filamentary structure at the very beginning of the simulation, $t = 10\mu$s. All the filaments are inside the separatrix. In the simulated region, the mode number in the simulated domain is 3. The second and third slices show the inverse cascade of the toroidal structure and the mode number is changed from 3 to 2 due to the nonlinear wave-wave interactions. The fourth slice shows the nonlinear filaments of the ELM at $t = 100\mu$s. At this time, the positive perturbations, shown as the red color, moves outwards and located outside the separatrix. At this time, the real ELM filaments move into the SOL and the energy stored in the filaments is transported along the magnetic field line to the divertor targets.

Figure 10(a) shows the time evolution of the toroidal mode structures of the parallel heat fluxes in the simulated domain at inner plate (top panel), outer plate (middle panel) and outer mid-plane (bottom panel). At the beginning of the simulation, the toroidal mode number in the simulated domain is set to be 24, as the dominant mode at the outer mid-plane and the other modes, from 0 up to 128 are set to be sub-dominant. Notice that the simulated domain is only 1/8 of the whole torus, thus the toroidal mode number labeled in Panel (a) is divided by 8. The time evolution of the kinetic energy at different toroidal mode n is plotted in Panel (b) of Fig. 10, and magnetic energy in Panel (c). Both kinetic and magnetic energy show the similar

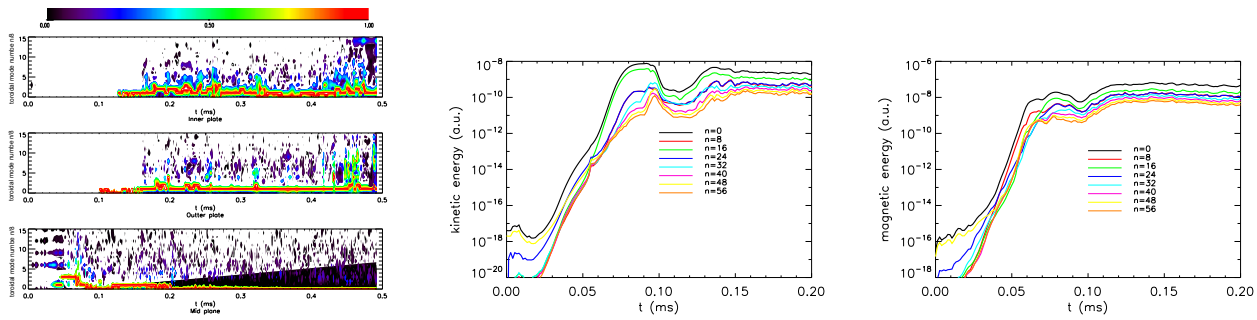

(a) (b) (c)

Figure 10: (a) The evolution of the toroidal mode structure of heat fluxes at inner plate (top), outer plate (middle) and outer mid-plane (bottom). The peak amplitudes are normalized to 1 for each time. (b) The time evolution of kinetic energy with different toroidal mode number n in the simulated domain. (c) The time evolution of magnetic energy with different toroidal mode number n.

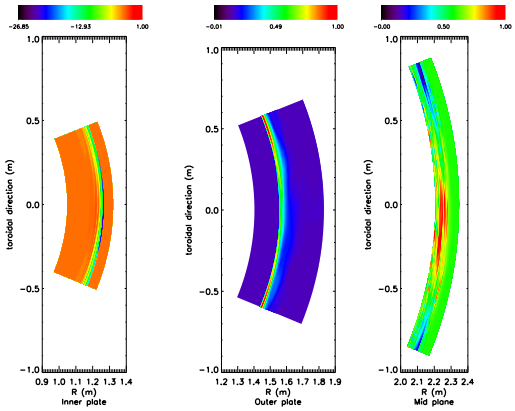

Figure 11: The heat flux on the toroidal plane at $t = 400\mu$s. The left panel is the heat flux distribution on the inner target. The middle one is at the out target and the left one is at outer mid-plane. The heat flux on targets shows the filamentary structure clearly. The positive peak amplitudes here are normalized to 1.

trends on different toroidal mode number. At the linear phase, the harmonics are excited, so the dominant mode is 48 in the simulated domain, as shown in Panel (a). In Panel (b) and (c), the $n = 48$ is the dominant mode which is consistent with Panel (a). Compared to Fig. 2, this dominant mode is very close to the most unstable mode $n = 50$ from the linear analysis. This difference of the toroidal mode number is caused by the different toroidal segments which we chose for the linear and nonlinear simulations. During this time period, the perturbations are confined at the closed field line region and there is no heat flux arriving the targets. At $t = 50 \sim 60\mu$s, the ELM crashes and the simulated toroidal mode number 1 becomes the dominant mode for a very short period and then changes to 3 (or $n = 24$ for the toroidal mode number) due to cascade. During this period, the energy starts to transport out of the separatrix. After $t \sim 70\mu$s, the inverse cascade precess of electric potential becomes more important and the dominant mode number is changed to 1 and then to 0. This process indicates that the nonlinear wave-wave interactions are more important during the ELM crash than the linear behavior [10]. At this time, thermal energy is transported along the magnetic field lines towards two divertor targets, but not reached yet. At the turbulence phase after $t \sim 200\mu$s, the zonal component is dominant and all the other modes are at the similar amplitude. The heat flux reached the outer target at $t \sim 100\mu$s and $\sim 130\mu$s at inner mid-plane, both with the dominant mode number 1. This shows that the burst of ELM mainly carries the energy to the divertor plates with the simulated toroidal mode number1 other than the dominant zonal component out of the separatrix.

Fig. 11 shows the simulated 2D heat flux distributions on the toroidal plane at $t = 400\mu$s. The x axises are the radial coordinate and the y axises are the toroidal direction. Compared to the distributions in Fig. 9 and which is plotted before 100μs, the mode number here is changed to 0 according to Fig. 10 due to the continuing inverse cascade. The heat flux towards inner plate is plotted at the left panel, and the middle panel is at outer target. The right panel is the heat flux distribution at outer mid-plane. In the left panel

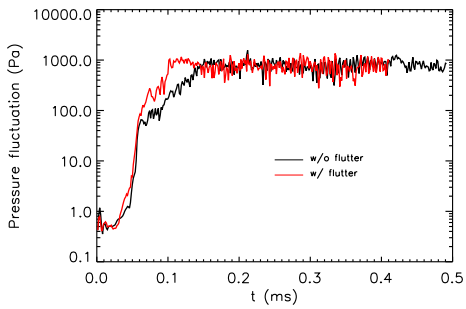

Figure 12: The time evolution of the growth of the pressure perturbation. The black curves are without the magnetic flutter terms in Eq. (13) and the red are with flutter terms. The magnetic flutter terms lead to larger energy loss, but do not affect the growth of the perturbation at linear phase.

the filamentary structures of the heat flux are shown as the yellow color on the orange background outside the inner separatrix where $R < 1.20$m. These footprint structures are generated due to ELM magnetic perturbations since the heat fluxes are mainly along the total magnetic field lines. At the outer target, the filamentary structures are not so obvious as that at inner target, because the strong ELM perturbations at LFS generate large radial ExB convection which dominates transport due to the magnetic flutter. Thus, the heat fluxes along the field lines towards target are not able to show the filamentary structures clearly. The heat flux distribution at outer mid-plane in the left panel is mainly inside the separatrix where $R_{sep} = 2.27$m. This figure intuitively tells that most of the heat flux is confined inside the separatrix, only a small part ($\sim 2\%$ as in Fig. 3(a)) is blown out by ELMs into the SOL. The heat flux in the SOL is transported along field lines towards the divertor targets and distributed over an area near the strike point, but most in the SOL. The amplitude of heat flux in private flux region is relatively very small.

5 Effects of magnetic flutter in parallel thermal conduction

As discussed in Ref. [29], the magnetic flutter has strong impact on the distribution of heat fluxes towards divertor targets. Here we try to use our model to understand this effect during the ELM crash event. As mentioned in Sec. 2, only the equilibrium parallel operator is kept in the calculations of thermal conduction in the previous simulations. If all the terms are kept, then the thermal conduction in Eq. (4) and (5) can be written as

$$\begin{aligned}\nabla_{\parallel}\left(\kappa_{\parallel j}\nabla_{\parallel}T_j\right) &= \nabla_{\parallel 0}\left(\kappa_{\parallel j}\nabla_{\parallel 0}T_{j1}\right)\\ &\quad +\mathbf{b}_0\times\nabla\psi\cdot\nabla\left(\kappa_{\parallel j}\nabla_{\parallel 0}T_{j1}\right)+\nabla_{\parallel 0}\left(\kappa_{\parallel j}\mathbf{b}_0\times\nabla\psi\cdot\nabla T_j\right)\\ &\quad +\mathbf{b}_0\times\nabla\psi\cdot\nabla\left(\kappa_{\parallel j}\mathbf{b}_0\times\nabla\psi\cdot\nabla T_j\right). \qquad (13)\end{aligned}$$

The second, third and fourth terms are generated due to the direction of perturbed magnetic field. Although this perturbation is considered in all the other terms in Eq. (1) - (5), it is neglected in the parallel thermal conduction in the previous work because of concerns about numerical pollution due to the extreme anisotropy between parallel (to the magnetic field) and perpendicular directions ($\kappa_{\parallel}/\kappa_{\perp} \sim 10^{10}$ in fusion plasmas) [16]. Here with the appropriate differential scheme in the operator, we get the ability to study the effects of the magnetic flutter in parallel thermal conduction.

Through the nonlinear simulations, the magnetic flutter terms are found to increase the total energy loss, or ELM size by 30%. The growing of the pressure fluctuation is plotted in Fig. 12. Compared with the two cases, both the black and red curves are almost overlapped at the linear phase, especially during $t \sim 0.04 - 0.06$ms, so the introduction of the magnetic flutter terms in parallel thermal conduction does not affect the linear growth rate. After $t \sim 0.06$ms, the fluctuation with flutter becomes larger than the case without it, and this leads to the larger energy loss. The fluctuation with flutter reaches its saturation value at $t \sim 0.1$ms and is much later at $t \sim 0.15$ms if without the magnetic flutter. During this period, the difference of the energy loss between two cases is enlarged since the larger fluctuations makes more energy to get out of the pedestal region.

The comparisons of the profiles at $t = 267\mu$s affected by the magnetic flutter terms are plotted in Fig. 13. The comparison of the n_e profiles are plotted in Panel (a), T_i in Panel (b) and $T_e$in Panel (c). The black

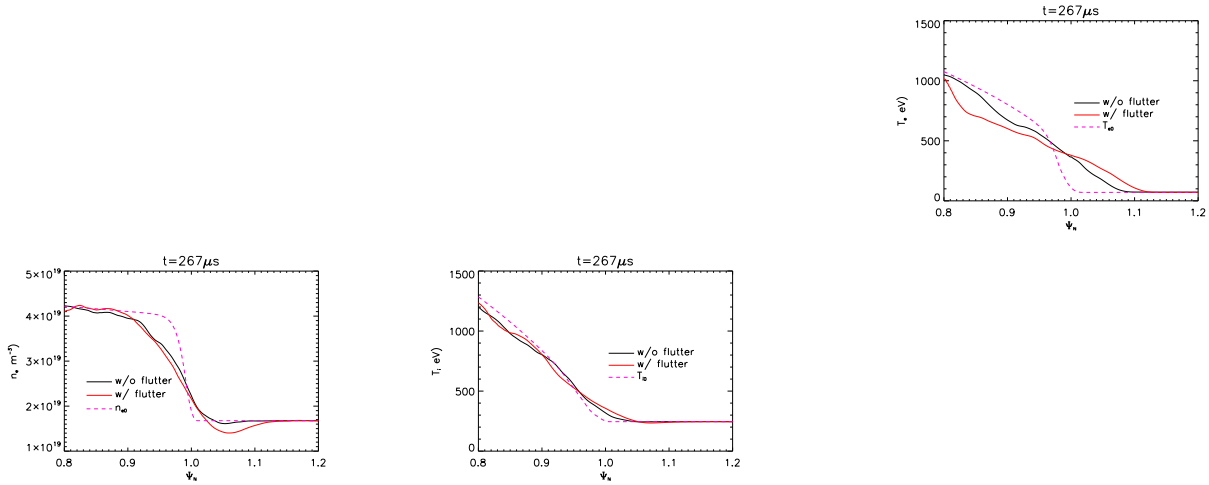

(a) (b) (c)

Figure 13: (a): The density profiles with and without magnetic flutter. (b): The ion temperature profiles. (c): The electron temperature profiles. The black curves are without the magnetic flutter terms and the red are with flutter. The magenta dashed curves means the equilibrium profile. The dashed magenta curves means the initial profiles in our simulations which are derived from experimental measurements.

curves are for the previous simulation without magnetic flutter terms in parallel thermal conductions and the red curves are with flutter. The dashed magenta curves means the equilibrium profiles at the beginning of the simulation. It is obvious that T_e profile is the most affected by the flutter terms since $\kappa_{eff,e}$ is much larger than $\kappa_{eff,i}$, while n_e and T_i are not dramatically changed by flutter terms. The introduction of the magnetic flutter terms increases the radial energy transport, which leads to the relaxation of the gradient of T_e profile. Therefore, in Panel (c), the profile with flutter is much broader than the without case at the pedestal region.

The magnetic flutter terms in thermal conduction are able to broaden the radial distribution of parallel heat flux to the targets. Fig. 14 shows the comparison of the heat flux towards the targets with and without magnetic flutter at 200μs after the start of the ELM crash. The red curves are for the case with flutter terms and black are for the case without it. In Panel (a), the red curve at outer target is wider than the black curve. For the case with flutter, although the peak value at strike point is higher, the heat flux drops suddenly from $\sim 1000\text{W/cm}^2$ to $\sim 400\text{W/cm}^2$ and stay around this value from $R \sim 1.58$m to 1.68m. The amplitude of the red curve is smaller than the black at $R \sim 1.57 - 1.62$m, and becomes larger from $R \sim 1.62$m. Therefore, we can say that the heat flux profile is really broadened over the outer target due to the enhancement of the radial transport induced by the magnetic flutter, so does the heat flux profile to inner target. Panel (b) is about the time evolution of the heat fluxes towards both inner and outer targets. The dashed curves are for the inner target and the solid are for the outer one. The amplitudes of the heat fluxes in Panel (b) are measured at $R = 1.62$m for outer target and $R = 1.24$m at inner target, where $\Psi_N = 1.025$. Both the red curves start to increase earlier than the black curves since the magnetic flutter leads to more energy loss from the beginning of the ELM crash. This figure shows that the difference of the amplitude between two red curves is much smaller than the black, which represents that the energy loss at inner target is enlarged by the magnetic flutter. The introduction of the magnetic flutter terms enhances the total parallel thermal conduction in SOL, and the increase of the energy loss is shown as the two routes toward the targets: both radial profiles are broadened and heat flux level amplified.

Figure 15 shows the comparison of the wetted length λ_w between cases with and without flutter from the burst of ELM until the nonlinear saturation phase towards the inner and outer divertor. The wetted length is defined as[30]:

$$\lambda_w = \frac{\int q(t) dA}{2\pi R q_{max}(t)}, \tag{14}$$

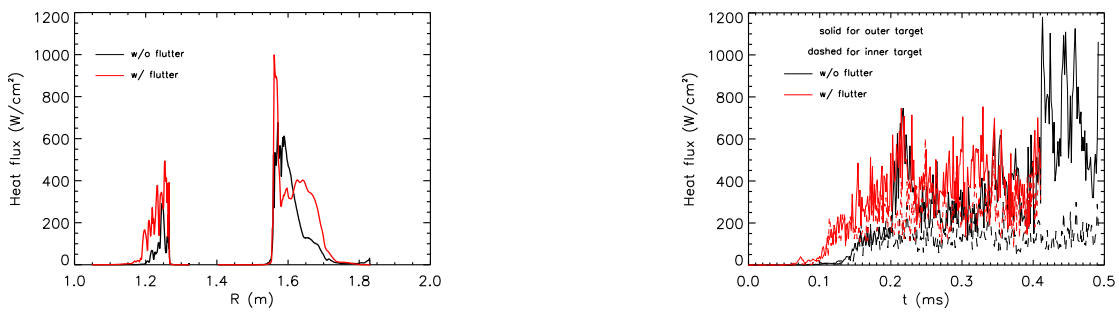

(a) (b)

Figure 14: (a): The comparison of the radial distribution of heat fluxes to divertor targets at 200μs after the beginning of the simulation with and without magnetic flutter terms. (b): The time evolution of the heat fluxes to targets. The dashed curves are for the inner target and the solid curves are for outer target. For both panels, black curves represent the case without magnetic flutter terms and red are with the terms. The magnetic flutter terms are able to enlarge the amplitude of the heat flux and widen the width.

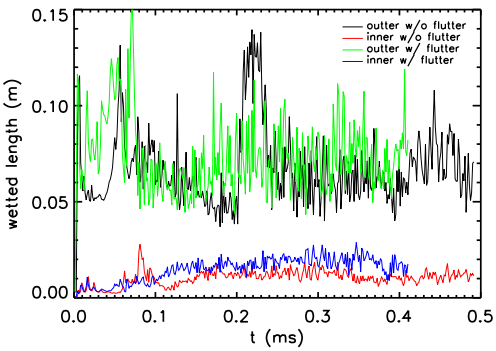

Figure 15: The time evolution of the wetted length λ_w at inner and outer boundary. The black curve is λ_w without magnetic flutter terms at outer target, and the red is the same case at inner target. The green and blue curves represent λ_w with flutter at outer and inner target respectively. The magnetic flutter terms are able to broaden λ_w especially at inner target.

where $q(t)$ and $q_{max}(t)$ are the local and maximum of the heat fluxes towards targets. The time averaged λ_w after $t = 0.1$ms without flutter terms is 0.067m at outer target and 0.012 at inner target, while this value is increased by magnetic flutter terms to 0.071m at outer target and 0.018m at inner target. The magnetic flutter broadens the width of the heat fluxes, especially at inner target. Therefore, the averaged wetted length are broadened by magnetic flutter by 50% at inner target and 6% at out target. This result is consistent with the analysis of Fig. 14(a). Compared to the measurements in Fig. 8(a), the heat flux distribution with magnetic flutter shows more similar peak position at $R \sim 1.65$m and more similar expansion from $R \sim 1.56$ to 1.70m on the outer target. For outer target, if without flutter, λ_w is broadened by 2.7 times due to the burst of ELM according to the amplitudes at the first highest peak at t 60μs and the valley before this time. If with flutter, λ_w is broadened by 1.6 times at t 70μs. Compared with the results of JOREK code in Fig. 4 of Ref. [30], our simulations in Fig. 14(b) and Fig. 15 show high frequency fluctuation because of multi toroidal modes kept in our model. The turbulence leads to such fluctuation.

The 2D distribution of the heat flux near the X-point on the poloidal cross section is shown in Fig. 16. In the both panels, the red color means the heat flux flowing in the clockwise direction on the poloidal cross section and the blue means counter-clockwise. The heat fluxes inside the separatrix are dominated by turbulent transport, and there is no definite poloidal direction. The E×B convection is important at the pedestal region and leads to such turbulent structure. The situation is opposite in the SOL, particularly in divertor region. The heat flux has clear directions and is towards the target near both inner and outer divertor since the parallel transport is dominant when outside the separatrix. The ELM bursts the energy out of the last closed surface at the outer mid-plane and the flux is transported along the field lines in the SOL, from the mid-plane at LFS to both targets. Compared to the inner target, there are several lobe structures near the outer target around the X-point. The influence of the magnetic flutter in thermal conduction is shown in the black circles in both panels. The lobe structures are broadened and elongated for the case with flutter. As Eq. (13) shows, the magnetic flutter in thermal conduction mainly acts on the direction perpendicular to the equilibrium magnetic field line, thus both radial and poloidal transport are enhanced. The elongation of the lobe structures near outer target is related with the broadening of the heat flux distribution towards target, as shown by the red curve in Fig. 14 (a). The second peak from the strike point at $R \sim 1.65$m is due to the long enough lobe structure which reaches the outer target.

6 Summary

In order to study the distribution and evolution of the transient heat flux during ELMy H-mode in divertor geometry in tokamaks, the electromagnetic six-field two-fluid model is revised. The nonideal physics effects, such as Spitzer resistivity, ion FLR effects, parallel thermal conductions, hyper-resistivity, etc., are taken into the consideration. The DIII-D ELMy H-mode discharge #144382 is used as the lower single-null equilibrium of the simulation. In this discharge, a small Type-I ELM at 2544.5ms was detected with multiple fast acquisition data chords in the pedestal, SOL and divertor. The heat flux profiles were also detected by the fast target heat flux measurements by IRTV at 12kHz. The linear analysis shows that this ELM is ideal MHD stable and destabilized by resistive-ballooning mode.

(a) (b)

Figure 16: The poloidal contour plots of the heat flux near X-point and divertor. Panel (a): The heat flux without magnetic flutter terms in the parallel thermal conduction. Panel (b): The heat flux with magnetic flutter. The comparison of the poloidal structures of heat flux shown in the circles shows that the lobe structure near X-point is longer and wider when flutter is considered.

The flux-limited expression plays as the kinetic modification from the classical Spitzer-Härm-Braginskii model of the parallel thermal conduction in SOL. Based on the precious research on flux limited coefficient α_j, it is set as a calibration parameter in our model. In order to validate with the measurements, three models of α_j are studied here. The larger α_j leads to larger conductive radial energy fluxes through both ion and electron channels. Therefore, the enlarged radial energy fluxes leads to the increase of the total ELM size since more energy is transported out of the separatrix and lost towards divertor targets in SOL. The 20 times difference of the α_j value of free-streaming from sheath limit model results in more than 6 times of the amplitudes of the heat fluxes towards both inner and outer targets, and the widths of the fluxes are also expanded. Since most of the energy loss is from the electron channel, the T_e profile becomes broader with larger α_j. To validate with the experimental measurements of DIII-D, the six-field two-fluid model with the sheath limit model of parallel thermal conduction are used, as it is able to get the closest total energy loss 18kJ during the burst of ELM to the measured value 17kJ. The evolution of the density profile during the burst of ELM is reproduced by this model. The collapse width and depth of n_e are well simulated at different time step. The increasing process of the profiles of the heat flux at divertor targets measured by IRTV is also simulated by this model. The simulated heat flux width is $\sim$ 40% narrower than the measurements and the amplitude is around two times larger because there are no recombination and radiation effects of neutrals near the targets considered in this model. The evolution of the heat fluxes towards targets is much faster in the simulation than the measurements because the lack of the auxiliary heating source in the model, which is able to constrain the speed of the energy loss at pedestal region and can be simulated by flux-driven boundary conditions. The implementation and coupling of the neutral module and the flux-driven boundary conditions will be our future work.

Magnetic flutter combined with parallel thermal conduction is found to be able to increase the total energy loss by $\sim$ 33% since the magnetic flutter terms provide the additional conductive radial heat transport. Thus the profiles get more flatten with magnetic flutter, especially for T_e, which also indicates more energy loss. The larger energy loss leads to larger amplitudes of the heat fluxes towards both inner and outer divertor targets. The heat flux profile at both inner and outer target is broadened obviously by magnetic flutter. The averaged wetted length during the saturation phase at inner boundary is increased by 50% by magnetic flutter and 6% at outer target. The lobe structures near X-point at LFS are both broadened and elongated due to the magnetic flutter.

Acknowledgement

We gratefully acknowledge Max Fenstermacher, Charles Lasnier and Lei Zeng (UCLA) for providing the pedestal profiles, IRTV heat flux and fast reflectometer profile data used in this work. This work was performed under the auspices of the U.S. Department of Energy by Lawrence Livermore National Laboratory under Contract DE-AC52-07NA27344, LLNL LDRD project 12-ERD-022, and LDRD project 11-ERD-058, This material is based upon work supported by the U.S. Department of Energy, Office of Science, Office of Fusion Energy Sciences. This work was supported by program of Fusion Reactor Physics and Digital Tokamak with the CAS "One-Three-Five" Strategic Planning , and the JSPS-NRF-NSFC A3 Foresight Program in the field of Plasma Physics (NSFC: No.11261140328 and NRF: No. 2012K2A2A6000443). It

was supported by the China Natural Science Foundation under Contract No.11405215 and 11405217, the National Magnetic Confinement Fusion Science Program of China under Contracts No. 2014GB106001 and 2013GB111002. LLNL-JRNL-665624

References

[1] E.J. Doyle, R.V. Budny, J.C. DeBoo, J.R. Ferron, G.L. Jackson, T.C. Luce, M. Murakami, T.H. Osborne, J.M. Park, P.A. Politzer, H. Reimerdes, T.A. Casper, C.D. Challis, R.J. Groebner, C.T. Holcomb, A.W. Hyatt, R.J. La Haye, G.R. McKee, T.W. Petrie, C.C. Petty, T.L. Rhodes, M.W. Shafer, P.B. Snyder, E.J. Strait, M.R. Wade, G. Wang, W.P. West, and L. Zeng, ,September 22nd IAEA Fusion Energy Conf. (Geneva, Switzerland), (2008).

[2] M. Keilhacker, G. Becker, K. Bernhardi, A. Eberhagen, M. ElShaer, G. FuBmann, O. Gehre, J. Gernhardt, G. v. Gierke, E. Glock, G. Haas, F. Karger, S. Kissel, O. Kluber, K. Kornherr, K. Lackner, G. Lisitano, G.G. Lister, J. Massig, H.M. Mayer, K. McCormick, D. Meisel, E. Meservey, E.R. Muller, H. Murmann, H. Niedermeyer, W. Poschenrieder, H. Rapp,, B. Richter, H. Rohr, F. Ryter, F. Schneider, S. Siller, P. Smeulders, F. Soldner, E. Speth, A. Stabler, K. Steinmetz, K.-H. Steuer, Z. Szymanski, G. Venus, O. Vollmer and F. Wagner, Plasma Phys. Control. Fusion **26** (1984) 49 .

[3] P.B. Snyder, N. Aiba, M. Beurskens, R.J. Groebner, L.D. Horton, A.E. Hubbard, J.W. Hughes, G.T.A. Huysmans, Y. Kamada, A. Kirk, C. Konz, A.W. Leonard, J. Lönnroth, C.F. Maggi, R. Maingi, T.H. Osborne, N. Oyama, A. Pankin, S. Saarelma, G. Saibene, J.L. Terry, H. Urano and H.R. Wilson, Nucl. Fusion **49**, 085035 (2009).

[4] H. Zohm, Plasma Phys. Control. Fusion **38** (1996) 105.

[5] A. Loarte et al., Proc. 23rd IAEA fusion energy conference, Daejeon, Korea (2010).

[6] R. Schneider, X. Bonnin, K. Borrass, D. P. Coster, H. Kastelewicz, et al., Contrib. Plasma Phys. **46** (2006) 3.

[7] T.D. Rognlien, D.D. Ryutov, N. Mattor, and G.D. Porter, Phys. Plasmas, **6**, (1999) 1851.

[8] D.P. Coster, A.V. Chankin, H.-J. Klingshirn, X. Bonnin, A. Kukushkin and A. Loarte, 40th EPS Conference on Plasma Physics, (2013) P1.104.

[9] X.Q. Xu, B.D. Dudson, P.B. Snyder, M.V. Umansky and H.R. Wilson, Phys. Rev. Lett. **105** (2010) 175005.

[10] P.W. Xi, X. Q. Xu and P.H. Diamond, Phys. Rev. Lett. **112** (2014) 085001.

[11] X. Q. Xu, J. F. Ma, and G. Q. Li, Phys. Plasmas, **21** (2014) 120704.

[12] T.Y. Xia, X.Q. Xu and P.W. Xi, Nucl. Fusion **53** (2013) 073009.

[13] C. H. Ma, X. Q. Xu, P. W. Xi and T. Y. Xia, Phys. Plasmas **22**, (2015) 010702.

[14] X.Q. Xu, P.W. Xi, A. Dimits, I. Joseph, M.V. Umansky, T.Y. Xia, B. Gui, S.S. Kim, G.Y. Park, T. Rhee, H. Jhang, P.H. Diamond, B. Dudson, P. B. Snyder, Phys. Plasmas, **20** (2013) 056113.

[15] X.Q. Xu, M.V. Umansky, B.D. Dudson and P.B. Snyder, Commun. Comput. Phys. 4 (2008) 949 .

[16] X.Q. Xu, B.D. Dudson, P.B. Snyder, M.V. Umansky, H. Wilson and T. Casper, Nucl. Fusion. **51**, (2011) 103040.

[17] P.W. Xi, X.Q. Xu, and P.H. Diamond, Phys. Plasmas **21**, (2014) 056110.

[18] P.W. Fundamenski, Plasma Phys. Controlled Fusion **47** (2005) R163.

[19] M.V. Umansky, A.M. Dimits, I. Joseph, J.T. Omotani and T.D. Rognlien, Journal of Nuclear Materials **463**, (2015) 506.

[20] P.W. Xi, X.Q. Xu, T.Y. Xia, W.M. Nevins and S.S. Kim, Nucl. Fusion **53** (2013) 113020.

[21] B.D. Dudson, M.V. Umansky, X.Q. Xu, P.B. Snyder, H.R. Wilson., Comput. Phys. Commun. **180**, (2009) 1467.

[22] M.E.Fenstermacher, X.Q. Xu, T.Y. Xia, T. D. Rognlien, M. Umansky, I. Joseph, C.J. Lasnier, T.H. Osborne and L. Zeng, 40th EPS Conference on Plasma Physics, (2013) P4.104.

[23] L.L. Lao et al., Fusion Sci. Technol. **48**, (2005) 968

[24] D. Tskhakaya, F. Subba, X. Bonnin, D. Coster, W. Fundamenski, R.A. Pitts, JET EFDA Contributors, Contrib. Plasma Phys. **48** (1–3) (2008) 89.

[25] D. Tskhakaya b, R.A. Pitts, W. Fundamenski, T. Eich, S. Kuhn, JET EFDA Contributors, Journal of Nuclear Materials **390 – 391** (2009) 335.

[26] A.M. Dimits, I. Joseph, M.V. Umansky, Phys. Plasmas **21** (2014) 055907.

[27] T.Y. Xia and X.Q. Xu, Phys. Plasmas **20** (2013) 052102.

[28] E. Havlickova, W. Fundamenski, D. Tskhakaya, G. Manfredi and D. Moulton, Plasma Phys. Control. Fusion **54** (2012) 045002.

[29] Y. Liang, et al., Phys. Rev. Lett. **110**, (2013) 235002.

[30] G.T.A. Huijsmans and A. Loarte, Nucl. Fusion **53** (2013) 123023.